




Effect of concentration of Nd³⁺ on the photoluminescence and ferroelectric properties of Bi_{4-x}Nd_xTi₃O₁₂ films

Yudong Xu¹, Kunzhuang Hu¹, Min Shi^{1*} , Ruzhong Zuo², Guannan Qiu¹, Zhuolin Si¹, and Enyang Men¹

¹School of Materials Science and Engineering, Hefei University of Technology, Hefei 230069, China

²School of Materials Science and Engineering, Anhui Polytechnic University, Wuhu 241004, China

Received: 5 February 2021

Accepted: 3 May 2021

Published online:
16 May 2021

© The Author(s), under exclusive licence to Springer Science+Business Media, LLC, part of Springer Nature 2021

ABSTRACT

Lead-free films of Bi_{4-x}Nd_xTi₃O₁₂ were deposited on Pt(111)/Ti/SiO₂/Si(100) substrate via spin-coating methods. It is shown that there are no secondary phases in the films of Bi_{4-x}Nd_xTi₃O₁₂ and clear interfaces between the films of Bi_{4-x}Nd_xTi₃O₁₂ and substrates when the films are annealed at 700 °C. And the films of Bi_{4-x}Nd_xTi₃O₁₂ also exhibit a blue light emission peak at 437 nm and a yellow light emission peak at 580 nm. There are narrower band gaps, greater values of dielectric constant and lower values of dielectric loss when the concentration of Nd³⁺ varies from 0 to 0.85. And the films of Bi_{4-x}Nd_xTi₃O₁₂ possess the minimum of band gap energy (2.67 eV). Moreover, the films of Bi_{4-x}Nd_xTi₃O₁₂ exhibit minimal leakage current density and maximal remanent polarization, which is highly beneficial for the potential applications in multi-functional devices.

1 Introduction

Since the ferroelectricity in Rochelle salt crystals was discovered by French Valasek in 1920, ferroelectric materials have become a research hotspot [1] and been widely used in transducers, filters, resonators, ferroelectric memories and other fields [2–6]. Up to date, the widely used ferroelectric materials are lead-based because of their stable and excellent ferroelectric properties [7–10]. However, lead-based ferroelectric materials undesirably bring about harm to human beings and pollution to environment during

the preparation and application processes. As a result, researchers have been looking for alternative lead-free ferroelectric materials with good ferroelectricity to rival the lead-based ferroelectrics such as PbZr_xTi_{1-x}O₃ [11].

Bismuth titanate (Bi₄Ti₃O₁₂), a typical lead-free multiferroics, has drawn widespread attention owing to its high Curie temperature and excellent fatigue resistance [12–14]. Unfortunately, its remnant polarization is rather low because of the evaporation of Bi³⁺, which gives rise to the increase in concentration of oxygen vacancies and the deterioration of

Address correspondence to E-mail: hfutdou@hotmail.com

ferroelectricity [15]. Thus, more and more researchers have been trying to inhibit the evaporation of Bi^{3+} through doping of rare elements in $\text{Bi}_4\text{Ti}_3\text{O}_{12}$ [16–18]. M. Chen [19] reported that the substitution of Pr^{3+} for Bi^{3+} will decrease the space charge density which improves ferroelectric properties of $\text{Bi}_4\text{Ti}_3\text{O}_{12}$ materials. And C. P. Cheng [20] reported that the doping of Dy^{3+} will enhance the ferroelectricity of $\text{Bi}_4\text{Ti}_3\text{O}_{12}$. U. Chon [21] and X. Y. Mao [22] pointed that the doping of Nd^{3+} in $\text{Bi}_4\text{Ti}_3\text{O}_{12}$ can also enhance the ferroelectric properties. The reason is that the substitution of Nd^{3+} for Bi^{3+} causes obvious structural distortion along C axis, thus resulting in a large polarization along C axis [21, 23] besides inhibiting evaporation of Bi^{3+} . Surprisingly, $\text{Bi}_4\text{Ti}_3\text{O}_{12}$ materials doped with rare earth elements possess obvious photoluminescence [24, 25]. R. Bokolia [26] reported that Er^{3+} -doped $\text{Bi}_4\text{Ti}_3\text{O}_{12}$ materials possess photoluminescence besides ferroelectricity. And K. Ruan [27] maintained that Eu^{3+} -doped films of $\text{Bi}_4\text{Ti}_3\text{O}_{12}$ possess good photoluminescence. Although, up to date, ferroelectricity of Nd^{3+} -doped films of $\text{Bi}_4\text{Ti}_3\text{O}_{12}$ has been investigated [28, 29], there are a few reports on investigating photoluminescence of Nd^{3+} -doped films of $\text{Bi}_4\text{Ti}_3\text{O}_{12}$ [30, 31]. Therefore, it is necessary to investigate not only ferroelectricity but also photoluminescence of Nd^{3+} -doped films of $\text{Bi}_4\text{Ti}_3\text{O}_{12}$ systematically.

In this work, the films of $\text{Bi}_{4-x}\text{Nd}_x\text{Ti}_3\text{O}_{12}$ were prepared on the substrates (Pt(111)/Ti/SiO₂/Si(100)) via the sol–gel and spin-coating method. And impact of the concentration of Nd^{3+} in $\text{Bi}_{4-x}\text{Nd}_x\text{Ti}_3\text{O}_{12}$ films on the ferroelectric properties, dielectric properties, leakage current densities and photoluminescence was investigated. Photoluminescence and ferroelectric properties were studied in detail.

2 Experimental

The films of $\text{Bi}_{4-x}\text{Nd}_x\text{Ti}_3\text{O}_{12}$ (when $x = 0, 0.25, 0.45, 0.65, 0.85$) were deposited on the Pt(111)/Ti/SiO₂/Si(100) substrate. And precursors were fabricated by sol–gel method. Neodymium oxide (Nd_2O_3), bismuth nitrate pentahydrate ($\text{Bi}(\text{NO}_3)_3 \cdot 5\text{H}_2\text{O}$) and tetrabutyl titanate ($\text{Ti}(\text{OC}_4\text{H}_9)_4$) were selected as starting materials. 2-methoxyethanol ($\text{C}_3\text{H}_8\text{O}_2$) and acetic acid ($\text{C}_2\text{H}_4\text{O}_2$) were used as the solvents. Acetylacetone ($\text{C}_5\text{H}_8\text{O}_2$) was used to stabilize the solution. Firstly, certain proportion of Nd_2O_3 and $\text{Bi}(\text{NO}_3)_3 \cdot 5\text{H}_2\text{O}$ was

dissolved in $\text{C}_2\text{H}_4\text{O}_2$ according to the stoichiometry of $\text{Bi}_{4-x}\text{Nd}_x\text{Ti}_3\text{O}_{12}$. Thus, solution A was obtained. And excessive $\text{Bi}(\text{NO}_3)_3 \cdot 5\text{H}_2\text{O}$ (8 wt%) was used to compensate volatilization of Bi^{3+} during annealing process. Then, $\text{Ti}(\text{OC}_4\text{H}_9)_4$ was dissolved in $\text{C}_3\text{H}_8\text{O}_2$, and a small quantity of stabilizer ($\text{C}_5\text{H}_8\text{O}_2$) was dripped into $\text{C}_3\text{H}_8\text{O}_2$. Then, solution B was obtained. Then, the above two solutions were mixed to get a sol. And the sol was deposited on the substrates to get monolayered films of $\text{Bi}_{4-x}\text{Nd}_x\text{Ti}_3\text{O}_{12}$ via spin-coating technology. Subsequently, the films of $\text{Bi}_{4-x}\text{Nd}_x\text{Ti}_3\text{O}_{12}$ were pre-annealed and annealed in tube furnace. At last, the above-mentioned process needs to be repeated three times to acquire four-layered films of $\text{Bi}_{4-x}\text{Nd}_x\text{Ti}_3\text{O}_{12}$. The flowchart of preparation is displayed in Fig. 1.

The phase constitutions of the films of $\text{Bi}_{4-x}\text{Nd}_x\text{Ti}_3\text{O}_{12}$ were carried out by X-ray diffraction (X'Pert Pro MPD, PANalytical, Holland). The morphologies of the surface and cross-section were investigated through FESEM (SU8020, Hitachi, Japan). Ag dot electrodes with thickness of 100 nm and diameter of 1 mm were deposited on the surface of the films through vacuum evaporation coater (HFJS-DZ300, JieShuo, P. C. China). P-E hysteresis loops of the films were determined by Precision LC Unit (Radiant Precision LC, Radiant Technologies, USA). The leakage current densities were determined by semiconductor tester (4200-SCS, Keithley, USA). Absorption spectrum of films was obtained by the UV spectrophotometer (Cary-5000, Agilent, USA). Photoluminescent spectrum of the films was measured via fluorescence spectrophotometer (F4500, Hitachi, Japan).

3 Results and discussion

3.1 Phase constitution

The XRD patterns of the five films of $\text{Bi}_{4-x}\text{Nd}_x\text{Ti}_3\text{O}_{12}$ are displayed in Fig. 2. As shown in Fig. 2a, it is obvious that the diffraction peaks of the films of $\text{Bi}_{4-x}\text{Nd}_x\text{Ti}_3\text{O}_{12}$ are composed of those from $\text{Bi}_4\text{Ti}_3\text{O}_{12}$ (JCPDS No.72–1019) and from Pt on the top layer of the substrates without any from impurity phases [32, 33]. It indicates that Nd^{3+} has dissolved into the crystal lattice of $\text{Bi}_4\text{Ti}_3\text{O}_{12}$ and pure films of $\text{Bi}_{4-x}\text{Nd}_x\text{Ti}_3\text{O}_{12}$ have been prepared [34, 35]. And the sharp peaks imply good crystallinity [26]. As shown

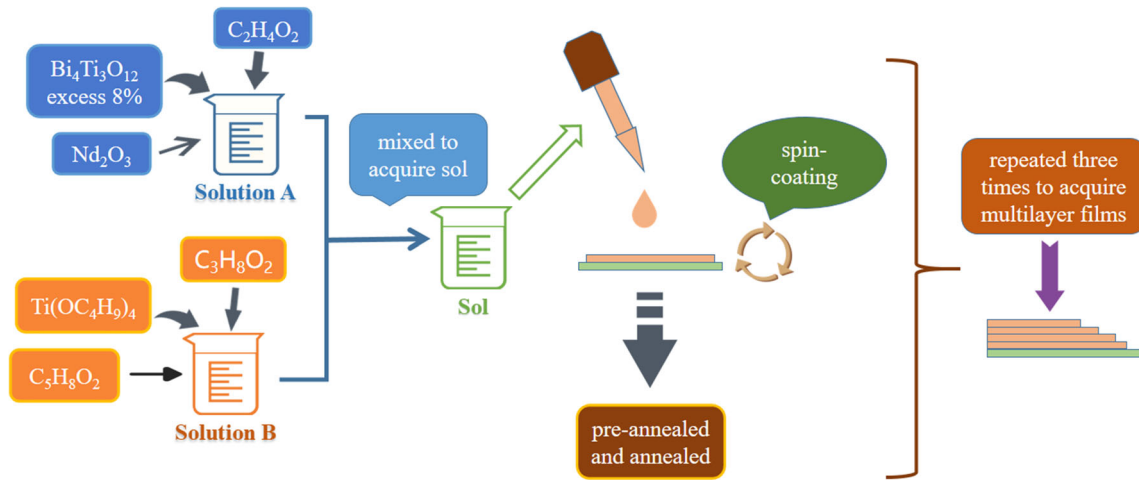


Fig. 1 The flowchart of preparation of $\text{Bi}_{4-x}\text{Nd}_x\text{Ti}_3\text{O}_{12}$ films

in Fig. 2b, for all the five films, the diffraction peaks at about 30.0° shift slightly to a greater angle. This is mainly due to the fact that the radius of Nd^{3+} (1.11 \AA) is less than that of Bi^{3+} (1.17 \AA) [22, 28]. The replacement of Bi^{3+} with Nd^{3+} will lead to reduction in lattice parameters and crystal plane spacing, which give rise to shift of the diffraction peaks to a greater angle according to Bragg equation.

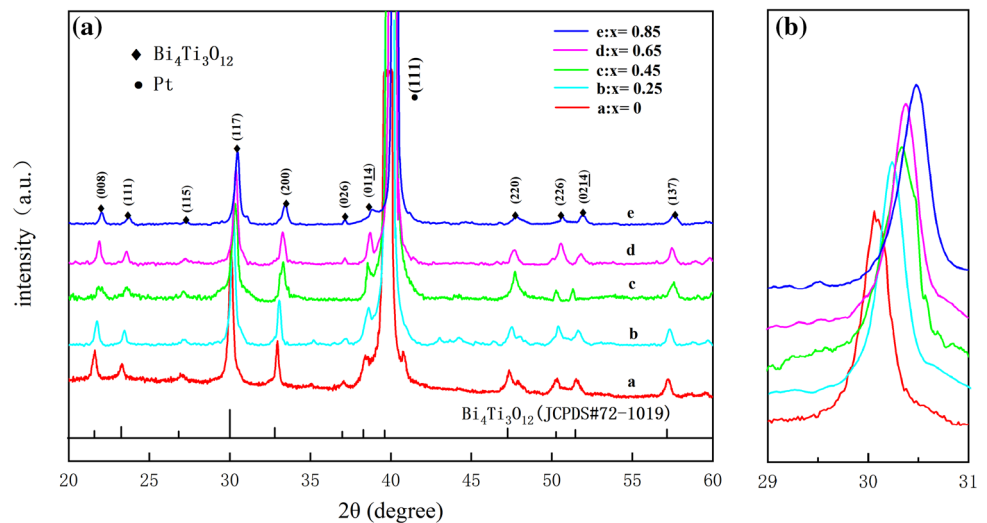
3.2 Microstructure

The FESEM morphologies of surface of the films are illustrated in Fig. 3. It is seen that, for the films of $\text{Bi}_{4-x}\text{Nd}_x\text{Ti}_3\text{O}_{12}$ (x being 0 and 0.25, respectively), there are obvious cracks and pores on the surfaces of these samples. However, for the other films, a few pores can be found. For five films, grain boundaries are not

be found. And there are polygonal particles without plate-like particles. And the average particle sizes of five films of $\text{Bi}_{4-x}\text{Nd}_x\text{Ti}_3\text{O}_{12}$ are listed in Table 1. With the increase in concentration of Nd^{3+} , the particle sizes decrease and the relative density of the films of $\text{Bi}_{4-x}\text{Nd}_x\text{Ti}_3\text{O}_{12}$ increases.

The FESEM morphologies of cross-section of the films of $\text{Bi}_{4-x}\text{Nd}_x\text{Ti}_3\text{O}_{12}$ are shown in Fig. 4. All the five films exhibit layered structure. The interfaces between the films of $\text{Bi}_{4-x}\text{Nd}_x\text{Ti}_3\text{O}_{12}$ and substrates are flat. And there are no inter-layers between the films and substrates, implying that no diffusion exists between the films of $\text{Bi}_{4-x}\text{Nd}_x\text{Ti}_3\text{O}_{12}$ and substrates. It can be observed that the thicknesses of the films of $\text{Bi}_{4-x}\text{Nd}_x\text{Ti}_3\text{O}_{12}$ are all around 200 nm, which is greater than that of pure films of $\text{Bi}_{4-x}\text{Nd}_x\text{Ti}_3\text{O}_{12}$. The difference in thicknesses for the films of Bi_{4-x}

Fig. 2 **a** The XRD patterns of $\text{Bi}_{4-x}\text{Nd}_x\text{Ti}_3\text{O}_{12}$ films; **b** magnified diffraction peaks at about 30.0°



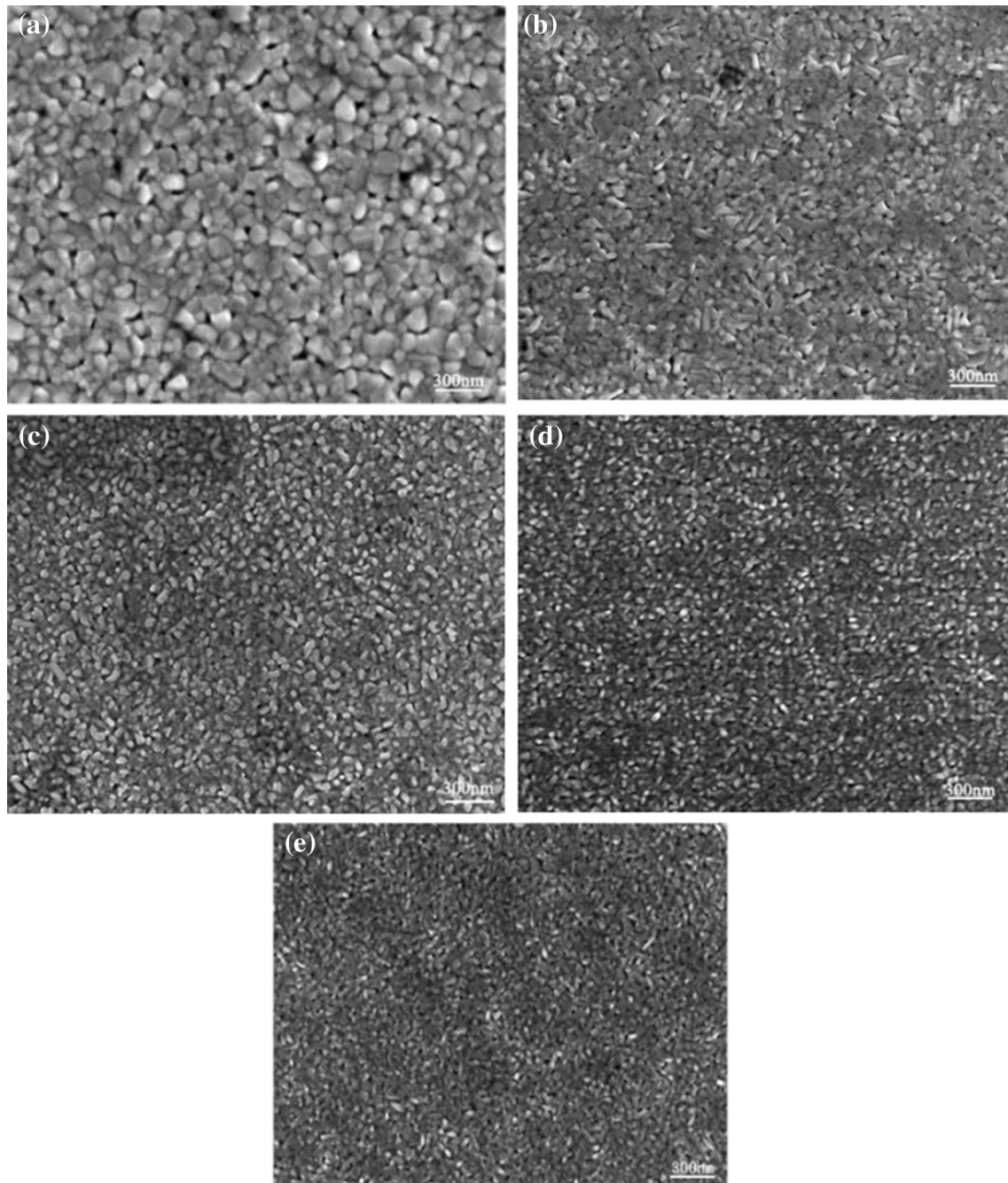


Fig. 3 The FESEM morphologies of surface of $\text{Bi}_{4-x}\text{Nd}_x\text{Ti}_3\text{O}_{12}$ films **a** $x = 0$; **b** $x = 0.25$; **c** $x = 0.45$; **d** $x = 0.65$; **e** $x = 0.85$

Table 1 The average particle sizes, ferroelectric parameters, leakage current densities and bandgap energy of $\text{Bi}_{4-x}\text{Nd}_x\text{Ti}_3\text{O}_{12}$ films

Concentration of Nd^{3+}	0	0.25	0.45	0.65	0.85
Particle size (nm)	148.3	98.4	95.7	91.0	89.2
Pr ($\mu\text{C}\cdot\text{cm}^{-2}$)	3.93	6.31	17.25	12.97	10.16
Ps ($\mu\text{C}\cdot\text{cm}^{-2}$)	12.62	19.03	50.56	38.81	35.13
Ec ($\text{KV}\cdot\text{cm}^{-1}$)	103.69	111.38	58.14	107.35	97.62
Leakage current density ($\times 10^{-6} \text{ A}\cdot\text{cm}^{-2}$)	18.5	6.09	1.02	3.05	4.84
Eg (eV)	–	3.05	2.88	2.79	2.67

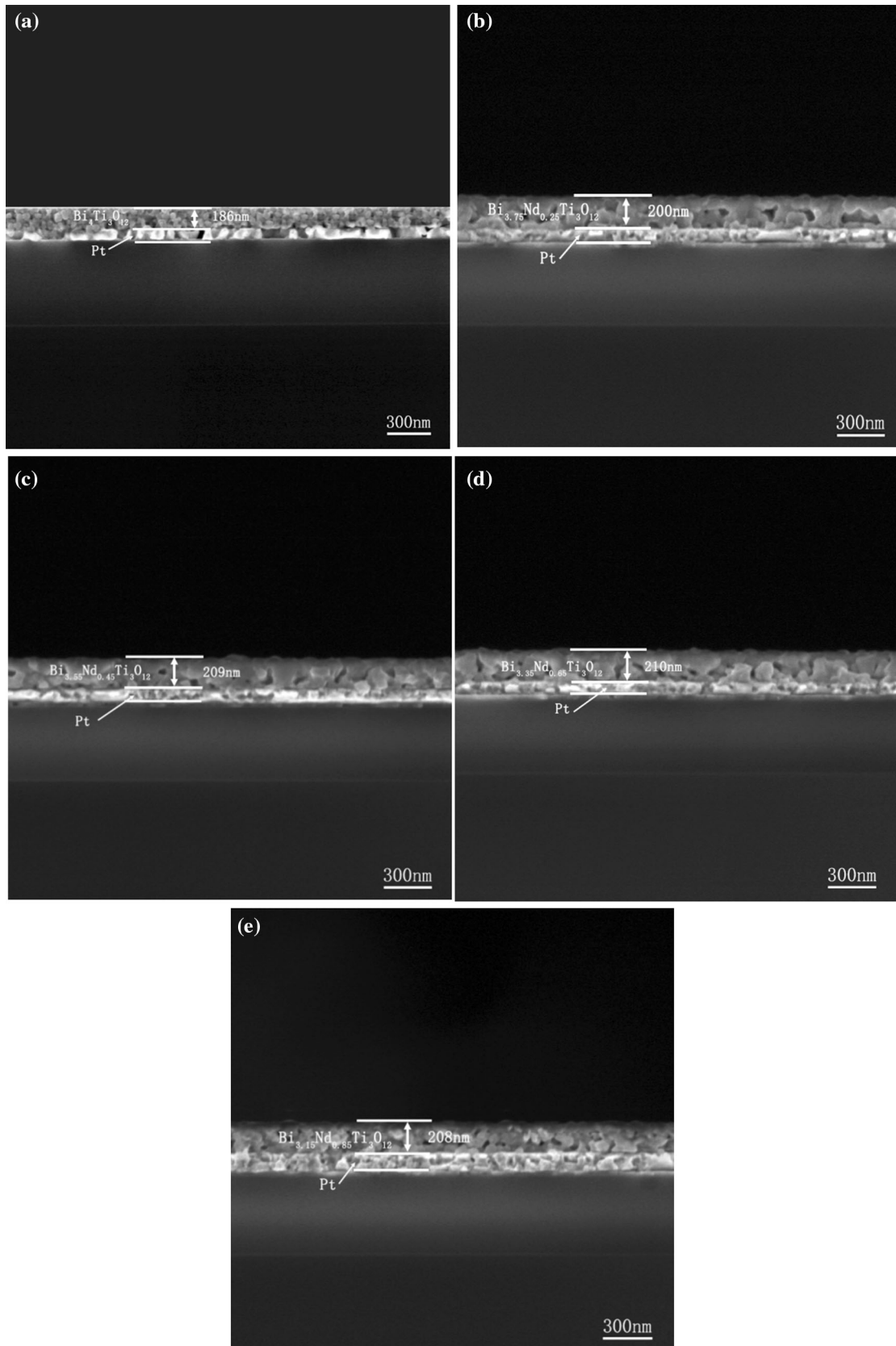


Fig. 4 The FESEM morphologies of cross-section of $\text{Bi}_{4-x}\text{Nd}_x\text{Ti}_3\text{O}_{12}$ films: **a** $x = 0$; **b** $x = 0.25$; **c** $x = 0.45$; **d** $x = 0.65$; **e** $x = 0.85$

$\text{Nd}_x\text{Ti}_3\text{O}_{12}$ with different concentration of Nd^{3+} is mainly due to the preparation of films by spin-coating technology.

3.3 Ferroelectric properties

The hysteresis loops of the films of $\text{Bi}_{4-x}\text{Nd}_x\text{Ti}_3\text{O}_{12}$ are displayed in Fig. 5. The results obtained from Fig. 5 are listed in Table 1. The films of $\text{Bi}_{4-x}\text{Nd}_x\text{Ti}_3\text{O}_{12}$ seem to exhibit good ferroelectricity. The values of remnant polarization (P_r) and saturated polarization (P_s) of the films of $\text{Bi}_{4-x}\text{Nd}_x\text{Ti}_3\text{O}_{12}$ are great than those of un-doped film of $\text{Bi}_4\text{Ti}_3\text{O}_{12}$ which indicates that doping of Nd^{3+} is beneficial for the improvement of the ferroelectric properties. It is seen that, firstly, the values of P_r increase to $17.25 \mu\text{C}\cdot\text{cm}^{-2}$ and then decrease gradually with increasing concentration of Nd^{3+} . The films of $\text{Bi}_{3.55}\text{Nd}_{0.45}\text{Ti}_3\text{O}_{12}$ possess the maximal value of P_r ($17.25 \mu\text{C}\cdot\text{cm}^{-2}$) which is greater than those films of $\text{Bi}_4\text{Ti}_3\text{O}_{12}$ in Ref. [28] ($10.5 \mu\text{C}\cdot\text{cm}^{-2}$), Ref. [36] ($10.5 \mu\text{C}\cdot\text{cm}^{-2}$), Ref. [38] ($10 \mu\text{C}\cdot\text{cm}^{-2}$) and Ref. [29] ($14.3 \mu\text{C}\cdot\text{cm}^{-2}$). And it is also significantly greater than un-doped film of $\text{Bi}_4\text{Ti}_3\text{O}_{12}$ in Ref. [38] ($4.8 \mu\text{C}\cdot\text{cm}^{-2}$).

In addition, it is worth noting that volatilization of Bi^{3+} during annealing process inevitably brings about increased oxygen vacancies and degraded ferroelectric properties of the films [32, 34]. The doping of a small amount of Nd^{3+} will inhibit the volatilization of Bi^{3+} and reduce the concentration of oxygen vacancies. As shown in Fig. 5, the values of

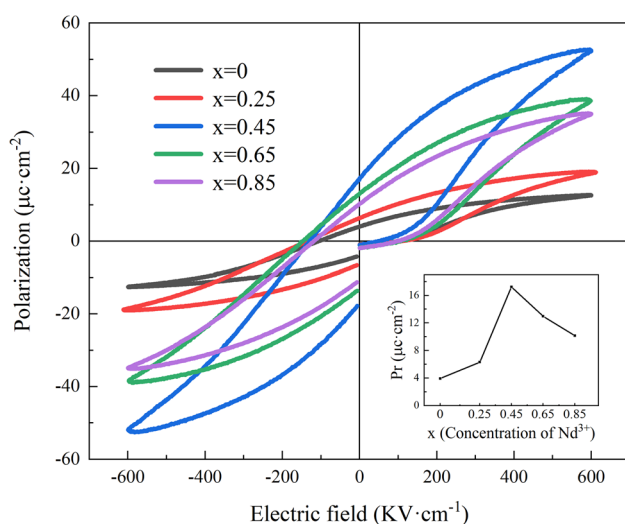


Fig. 5 The P - E hysteresis loops of $\text{Bi}_{4-x}\text{Nd}_x\text{Ti}_3\text{O}_{12}$ films; inset: the values of P_r of $\text{Bi}_{4-x}\text{Nd}_x\text{Ti}_3\text{O}_{12}$ films

P_r increase. However, with the further increase in the concentration of Nd^{3+} , particle size decreases and the values of P_r reduce correspondingly owing to the pinning effect [33, 37]. Therefore, the film of $\text{Bi}_{3.55}\text{Nd}_{0.45}\text{Ti}_3\text{O}_{12}$ possesses the maximal value of P_r .

3.4 Leakage current densities

The leakage current densities of the films of $\text{Bi}_{4-x}\text{Nd}_x\text{Ti}_3\text{O}_{12}$ are displayed in Fig. 6. Obviously, when the values of applied electric field (E) are below $100 \text{ kV}\cdot\text{cm}^{-1}$, the leakage current densities increase rapidly with increasing E . However, when the values of E are greater than $100 \text{ kV}\cdot\text{cm}^{-1}$, the leakage current densities increase slowly and remain constant finally. Compared with the film of $\text{Bi}_4\text{Ti}_3\text{O}_{12}$, Nd^{3+} -doped films possess lower leakage current densities, indicating that doping of Nd^{3+} is beneficial for the reduction in leakage current densities. The reason is that volatilization of Bi^{3+} during the annealing process induces higher concentration of oxygen vacancies [39]. And the substitution of Nd^{3+} for Bi^{3+} inhibits the volatilization of Bi^{3+} effectively, thus reducing oxygen vacancies and leakage current densities. The data summarized from Fig. 6 are shown in Table 1. Among the five films, the film of $\text{Bi}_{3.55}\text{Nd}_{0.45}\text{Ti}_3\text{O}_{12}$ possesses the minimum of leakage current density ($1.02 \times 10^{-6} \text{ A}\cdot\text{cm}^{-2}$), which is close to the data from Ref. [28] ($2 \times 10^{-6} \text{ A}\cdot\text{cm}^{-2}$) and lower than those from Ref. [40] ($1.15 \times 10^{-5} \text{ A}\cdot\text{cm}^{-2}$) and Ref. [29] ($2.0 \times 10^{-5} \text{ A}\cdot\text{cm}^{-2}$). It should be noted

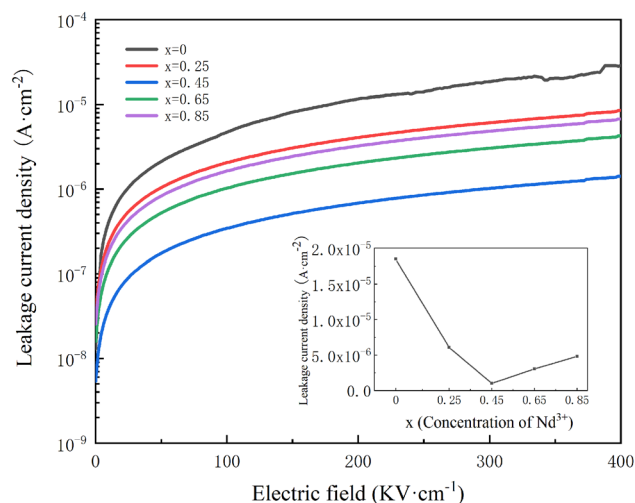


Fig. 6 The leakage current densities of $\text{Bi}_{4-x}\text{Nd}_x\text{Ti}_3\text{O}_{12}$ films under different electric field; inset: the leakage current densities of $\text{Bi}_{4-x}\text{Nd}_x\text{Ti}_3\text{O}_{12}$ films at $300 \text{ kV}\cdot\text{cm}^{-1}$

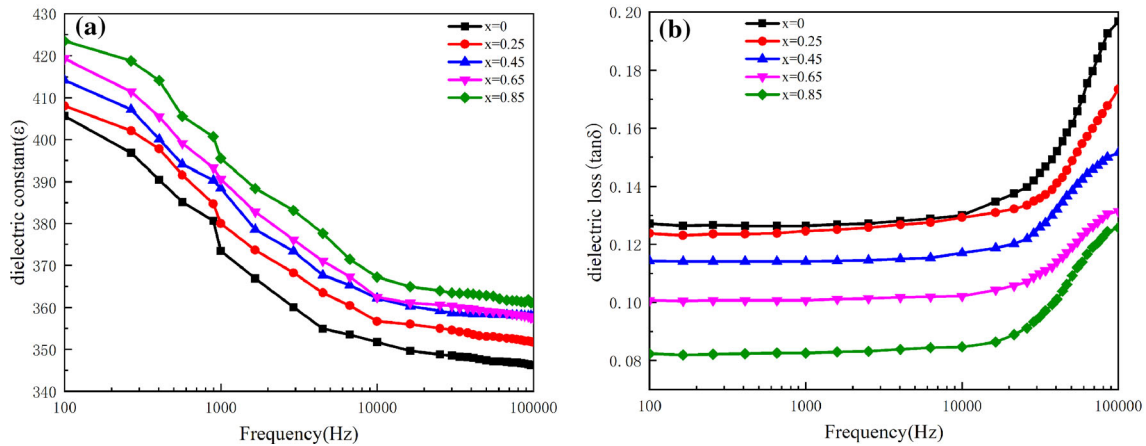


Fig. 7 **a** Variation of dielectric constant with frequency for $\text{Bi}_{4-x}\text{Nd}_x\text{Ti}_3\text{O}_{12}$ films; **b** variation of dielectric loss with frequency for $\text{Bi}_{4-x}\text{Nd}_x\text{Ti}_3\text{O}_{12}$ films

that leakage current density of the films of $\text{Bi}_{3.55}\text{Nd}_{0.45}\text{Ti}_3\text{O}_{12}$ is about one order lower than that of the film of $\text{Bi}_4\text{Ti}_3\text{O}_{12}$ ($1.85 \times 10^{-5} \text{ A}\cdot\text{cm}^{-2}$).

3.5 Dielectric properties

Variation of dielectric constant (ϵ) and dielectric loss ($\tan\delta$) with frequency is shown in Fig. 7. As shown in Fig. 7a, at lower frequency ($< 10,000 \text{ Hz}$), the values of ϵ decrease rapidly with increasing frequency. Nevertheless, at higher frequency ($> 10,000 \text{ Hz}$), the values of ϵ decrease slowly and remain nearly constant. The high values of dielectric constant at low frequency are due to the fact that the charges were trapped at interface states, which follows the alternating current variations [30]. And the space charge effect is suppressed at a higher frequency [30], thus the values of dielectric constant are greater at low frequency than those at high frequency. It is clearly seen from Fig. 7b that, with increasing frequency, the values of $\tan\delta$ remain nearly unchanged when frequency is smaller than $10,000 \text{ Hz}$ and increase rapidly when frequency is above $10,000 \text{ Hz}$. The significant increase in dielectric loss at high frequency may be ascribed to Maxwell–Wagner interfacial polarization or space charge polarization [31]. At the same frequency, the values of ϵ increase and the values of $\tan\delta$ decrease with the increasing concentration of Nd^{3+} . The structural inhomogeneity arising from Nd^{3+} doping breaks the translational symmetry which is not conducive to the coupling of electric dipoles. Thus, the concentration and the coupling of the dipoles decrease [41]. And dielectric

constant increases due to the doping of Nd^{3+} . The replacement of Bi^{3+} with Nd^{3+} inhibits the formation of oxygen vacancies [31]. And decrease in the values of dielectric loss with the increase in doping concentration of Nd^{3+} may be attributed to the reductions of concentrations of oxygen vacancy [42]. This indicates that doping of Nd^{3+} enhances the dielectric properties of the films effectively.

3.6 Photoluminescence

Excitation spectra of the films of $\text{Bi}_{4-x}\text{Nd}_x\text{Ti}_3\text{O}_{12}$ are shown in Fig. 8a. Obviously, there is a distinct excitation peak at about 294 nm which is close to the value of wavelength in Ref. [43] (292 nm). This position of wavelength corresponds to the energy level transition of $^4I_{9/2} \rightarrow ^2H_{11/2}$ [43, 44]. The emission spectra of the films of $\text{Bi}_{4-x}\text{Nd}_x\text{Ti}_3\text{O}_{12}$ are illustrated in Fig. 8b, showing that there is a blue light emission peak at 437 nm and one yellow light emission peak at 580 nm which are close to the values of wavelength in Ref. [43] (434 nm and 582 nm). These may be due to the energy level transitions of $^4G_{9/2} \rightarrow ^4F_{9/2}$ and $^4G_{7/2} \rightarrow ^4F_{9/2}$, respectively [43, 44]. The values of wavelength of the emission peaks remain almost constant under different doping concentration of Nd^{3+} . With increasing concentration of Nd^{3+} , the emission intensities increase firstly and then decrease. The emission intensity reaches the maximum when the concentration of Nd^{3+} is equal to 0.45 , which indicates quenching concentration is about 0.45 . Concentration quenching mechanism is highly relevant to the critical interaction distance

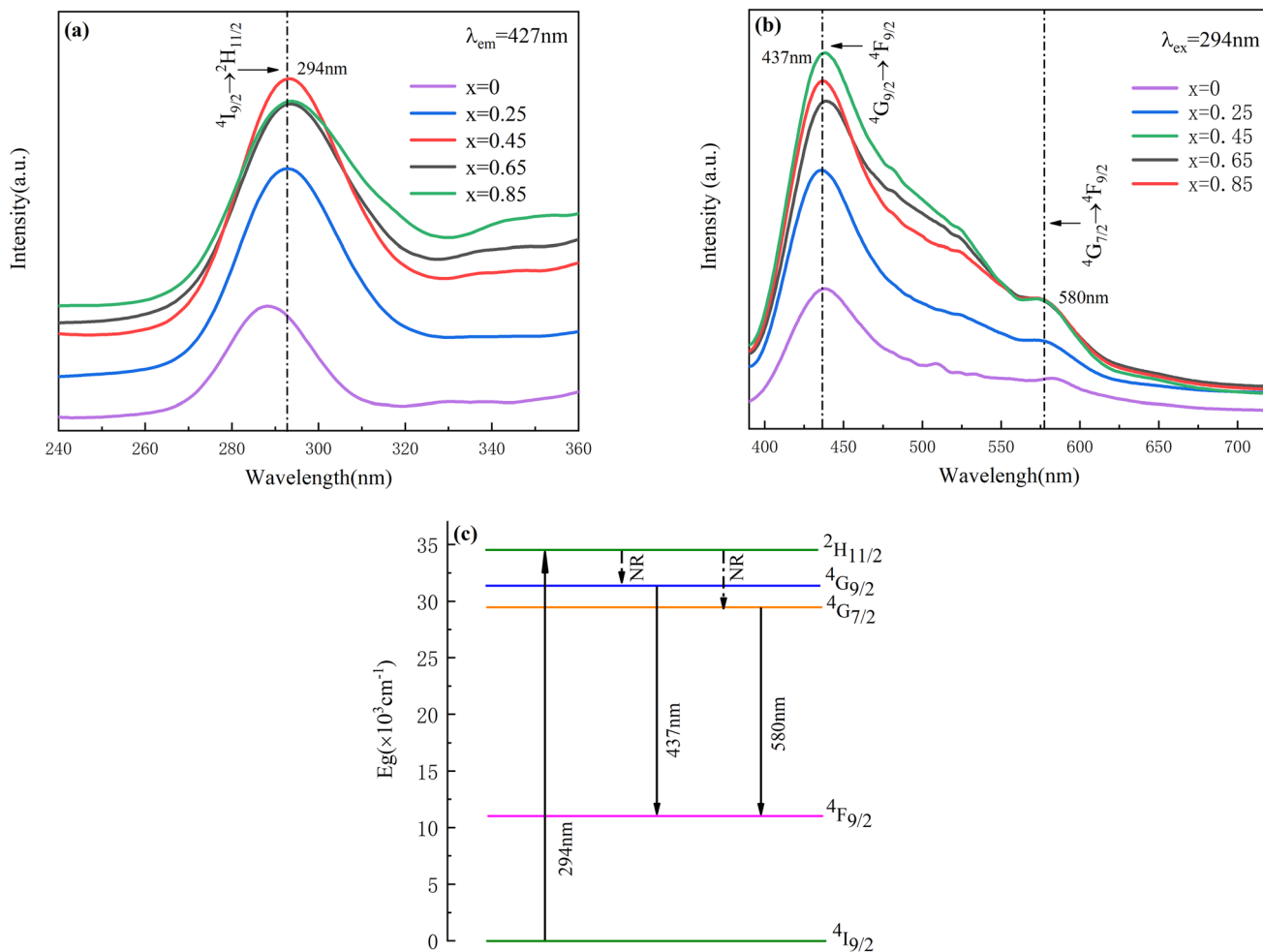


Fig. 8 **a** The excitation spectra of $\text{Bi}_{4-x}\text{Nd}_x\text{Ti}_3\text{O}_{12}$ films with different doped concentration of Nd^{3+} ; **b** the emission spectra of $\text{Bi}_{4-x}\text{Nd}_x\text{Ti}_3\text{O}_{12}$ films with different doped concentration of Nd^{3+} ; **c** partial energy level diagram of Nd^{3+}

between neighboring activators in the host lattice [45, 46].

Next, we give an intuitive description on the luminescence mechanism of the films of $\text{Bi}_{4-x}\text{Nd}_x\text{Ti}_3\text{O}_{12}$ based on the possible partial energy level diagram of Nd^{3+} , as shown in Fig. 8c. It can be clearly seen that Nd^{3+} was excited from ground state ($4I_{9/2}$) to excited state ($2H_{11/2}$) when excited at a deep ultraviolet light (DUV, 294 nm). Then, Nd^{3+} was relaxed from excited state of $2H_{11/2}$ to the energy level of $4G_{9/2}$ and $4G_{7/2}$ via non-radiative-relaxation [44, 46]. Finally, the electronic transitions from energy level of $4G_{9/2}$ and $4G_{7/2}$ to the energy level of $4F_{9/2}$ give rise to a blue light emission peak at 437 nm and a yellow light emission peak at 580 nm, respectively.

The diagrams of Commission Internationale de L'Eclairage (CIE) chromaticity coordinate of the films of $\text{Bi}_{4-x}\text{Nd}_x\text{Ti}_3\text{O}_{12}$ are shown in Fig. 9. It can be

found that CIE chromaticity coordinates of $\text{Bi}_{3.75}\text{Nd}_{0.25}\text{Ti}_3\text{O}_{12}$, $\text{Bi}_{3.55}\text{Nd}_{0.45}\text{Ti}_3\text{O}_{12}$, $\text{Bi}_{3.35}\text{Nd}_{0.65}\text{Ti}_3\text{O}_{12}$ and $\text{Bi}_{3.15}\text{Nd}_{0.85}\text{Ti}_3\text{O}_{12}$ are (0.2568, 0.2545), (0.2402, 0.2552), (0.2509, 0.2610), (0.2499, 0.2688), respectively. The CIE coordinates are located in the blue region of CIE diagram, as a contrast, CIE coordinates of nanometer powder prepared in Ref. [30] are in the green-yellow region.

The ultraviolet (UV) -visible (Vis) -near infrared (NIR) absorption spectra of the films of $\text{Bi}_{4-x}\text{Nd}_x\text{Ti}_3\text{O}_{12}$ are shown in Fig. 10a. It can be seen that the films exhibit obvious absorptions from 350 to 500 nm. In general, for the indirect transitions, the band gap energy (E_g) can be obtained via following formula [47, 48]:

$$\alpha h\nu^{1/2} = A(h\nu - E_g) \quad (1)$$

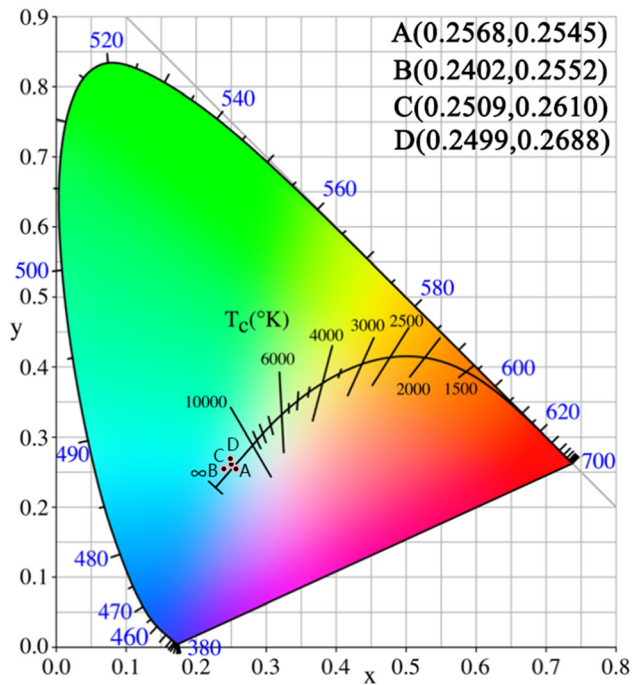


Fig. 9 The diagrams of CIE chromaticity coordinate of $\text{Bi}_{4-x}\text{Nd}_x\text{Ti}_3\text{O}_{12}$ films

where α is absorption coefficient from the absorption spectrum, A is constant and $h\nu$ is energy of a photon, respectively. Variations of $(\alpha h\nu)^{1/2}$ with $h\nu$ of the films are shown in Fig. 10b. The values of E_g are determined from the intersections of the curve tangent and the abscissa [49, 50], as shown in Table 1. Apparently, the values of E_g decrease gradually with the increasing concentration of Nd^{3+} , which is beneficial for enhancing visible light catalytic activity [47, 49]. It is reported that the doping of Nd^{3+} gives rise to the

distortions of TiO_6 octahedra [42], which is a dominating reason for reducing band gap energy [31]. Therefore, the value of E_g decreases with the increase in Nd^{3+} concentration. The value of E_g of the film of $\text{Bi}_{3.15}\text{Nd}_{0.85}\text{Ti}_3\text{O}_{12}$ is 2.67 eV, which is smaller than that reported in Ref. [47] (2.82 eV). The narrowed band gaps imply the potential application in light catalytic fields as smaller E_g is beneficial for enhancing visible light catalytic activity [47, 49].

4 Conclusions

The films of $\text{Bi}_{4-x}\text{Nd}_x\text{Ti}_3\text{O}_{12}$ doped with different concentrations of Nd^{3+} were deposited on the substrate via spin-coating technology. The as-prepared films of $\text{Bi}_{4-x}\text{Nd}_x\text{Ti}_3\text{O}_{12}$ are pure and have a few pores and cracks on the surfaces of the films. The interfaces between the films of $\text{Bi}_{4-x}\text{Nd}_x\text{Ti}_3\text{O}_{12}$ and the substrates are clear and flat. The film of $\text{Bi}_{3.55}\text{Nd}_{0.45}\text{Ti}_3\text{O}_{12}$ possess the maximum of Pr ($17.25 \mu\text{cm}^{-2}$) and the minimum of leakage current density ($1.02 \times 10^{-6} \text{A}\cdot\text{cm}^{-2}$). With the increasing concentration of Nd^{3+} , the values of ϵ of the films increase and the values of $\tan\delta$ decrease. The films of $\text{Bi}_{4-x}\text{Nd}_x\text{Ti}_3\text{O}_{12}$ exhibit a blue light emission peak at 437 nm and a yellow light emission peak at 580 nm. With increasing concentration of Nd^{3+} , the values of E_g decrease gradually. For the film of $\text{Bi}_{3.15}\text{Nd}_{0.85}\text{Ti}_3\text{O}_{12}$, the value of band gap energy is 2.67 eV. The photoluminescence and ferroelectric properties of the film of $\text{Bi}_{3.55}\text{Nd}_{0.45}\text{Ti}_3\text{O}_{12}$ are, on the whole, good and helpful for the applications in multi-functional devices.

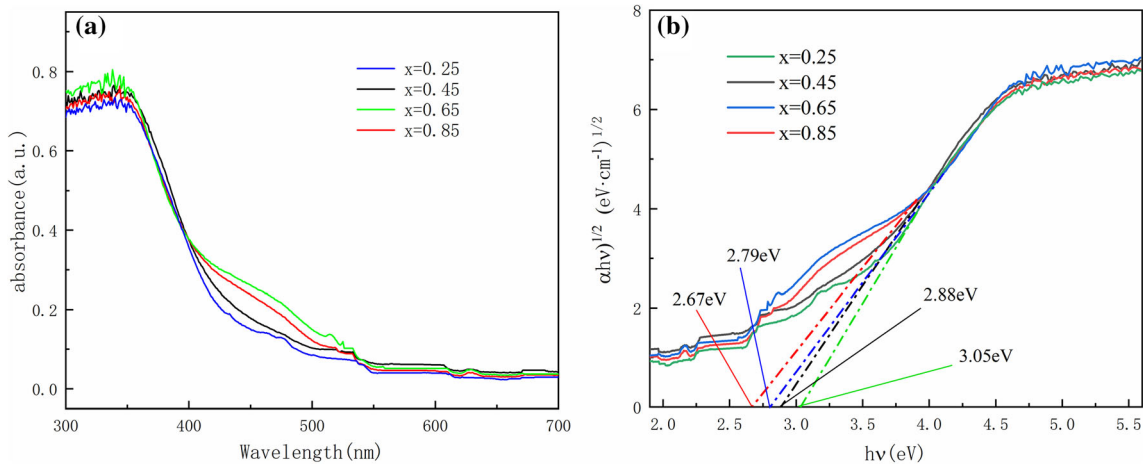


Fig. 10 a UV–Vis–NIR absorption spectra of $\text{Bi}_{4-x}\text{Nd}_x\text{Ti}_3\text{O}_{12}$ films; b variation of $(\alpha h\nu)^{1/2}$ with $h\nu$

Acknowledgements

The authors acknowledge the financial support from the National Natural Science Foundation of China (52072103).

Declarations

Conflict of interest The authors declare no conflict of interest.

References

- B. Fugiel, S. Komraus, T. Kikuta, Influence of side electric potential on hysteresis loop parameters and electric permittivity in the rochelle salt. *Phys. B* **407**, 3956–3959 (2012)
- W.T. Chen, A.E. Gurdal, S. Tuncdemir, J. Gambal, C.A. Randall, Introducing an extremely high output power and high temperature piezoelectric bimorph energy harvester technology based on the ferroelectric system Bi(Me)O₃-PbTiO₃. *J. Appl. Phys.* **128**, 144102 (2020)
- M.Z. Koochi, A. Mortazawi, Negative piezoelectric based electric-field-actuated mode-switchable multilayer ferroelectric FBARs for Selective control of harmonic resonances without degrading keff. *IEEE. T. Ultrason. Ferr.* **67**, 1922–1930 (2020)
- J. Wang, M. Park, S. Mertin, T. Pensala, F. Ayazi, A. Ansari, A film bulk acoustic resonator based on ferroelectric aluminum scandium nitride films. *J. Microelectromech. S.* **29**, 741–747 (2020)
- X. Qiao, W. Geng, D. Zheng, X. Chou, Robust in-plane polarization switching in epitaxial BiFeO₃ films. *J. Alloy. Compd.* **852**, 156988 (2020)
- P. Pandey, S.H. Wan, K.R. Udayakumar, T.S. Moise, A.C. Seabaugh, Programming-pulse dependence of ferroelectric partial polarization: insights from a comparative study of PZT and HZO capacitors. *IEEE. T. Electron. Dev.* **67**, 4482–4487 (2020)
- R. Indergand, A. Vidyasagar, N. Nadkarni, D.M. Kochmann, A phase-field approach to studying the temperature-dependent ferroelectric response of bulk polycrystalline PZT. *J. Mech. Phys. Solids.* **144**, 104098 (2020)
- S.A. Sharko, A.I. Serokurova, N.N. Novitskii, V.A. Ketsko, A.I. Stognij, Continuous ferrimagnetic Y₃Fe₅O₁₂ layers on the ceramic PbZr_{0.45}Ti_{0.55}O₃ substrates. *Ceram. Int.* **46**, 22049–22056 (2020)
- B. Gao, Z.H. Yao, D.Y. Lai, Q.H. Guo, W.G. Pan, H. Hao, M.H. Cao, H.X. Liu, Unexpectedly high piezoelectric response in Sm-doped PZT ceramics beyond the morphotropic phase boundary region. *J. Alloy. Compd.* **836**, 155474 (2020)
- P. Kumar, C. Prakash, Synthesis, dielectric and ferroelectric properties of Sm³⁺ modified PZTFN ceramics. *Mater. Chem. Phys.* **251**, 123061 (2020)
- H. Wang, H. Yuan, X. Liu, K. Wu, D. Lin, Achieving high energy-storage properties in Bi_{0.5}Na_{0.5}TiO₃-based lead-free ceramics under low electric fields. *Ceram. Int.* **47**, 1344–1352 (2020)
- M.A. Wederni, D.B. Jemia, H. Rahmouni, R.J. Martin-Palma, R. Chtourou, Structural, morphological, vibrational, and impedance properties of ytterbium modified bismuth titanate. *Chem. Phys. Lett.* **755**, 137787 (2020)
- M. Alguero, M. Perez-Cerdan, P.R.D. Real, J. Ricote, A. Castro, Novel aurivillius Bi₄Ti_{3-2x}Nb_xFe_xO₁₂ phases with increasing magnetic-cation fraction until percolation: a novel approach for room temperature multiferroism. *J. Mater. Chem. C.* **836**, 12457–12469 (2020)
- C.B. Long, H.Q. Fan, W. Ren, J.Y. Zhao, Double polarization hysteresis and dramatic influence of small compositional variations on the electrical properties in Bi₄Ti₃O₁₂ ceramics. *J. Eur. Ceram. Soc.* **39**, 4103–4112 (2019)
- R. Nie, J. Yuan, Q. Chen, J. Xing, J. Zhu, W. Zhang, Crystal distortion and electrical properties of Ce-doped BIT-based piezoelectric ceramics. *J. Am. Ceram. Soc.* **102**, 5432–5442 (2019)
- S. Ma, X.W. Cheng, T. Ali, Influence of tantalum on mechanical, ferroelectric and dielectric properties of Bi-excess Bi_{3.25}La_{0.75}Ti₃O₁₂ thin film. *Appl. Surf. Sci.* **463**, 1141–1147 (2019)
- C.Y. Yau, R. Palan, K. Tran, R.C. Buchanan, Mechanism of polarization enhancement in La-doped Bi₄Ti₃O₁₂ films. *Appl. Phys. Lett.* **86**, 032907 (2005)
- Y.Y. Wu, X.H. Wang, L.T. Li, Ferroelectric and dielectric properties of La/Mn co-doped Bi₄Ti₃O₁₂ ceramics. *Chinese Phys. B.* **19**, 037701 (2010)
- M. Chen, Z.L. Liu, Y. Wang, C.C. Wang, X.S. Yang, K.L. Yao, Ferroelectric properties of Pr₆O₁₁-doped Bi₄Ti₃O₁₂. *Solid. State. Commun.* **130**, 735–739 (2004)
- C.P. Cheng, M.H. Tang, Z. Ye, Y.C. Zhou, Ferroelectric properties of dysprosium-doped Bi₄Ti₃O₁₂ thin films crystallized in various atmospheres. *T. Nonferr. Metal. Soc.* **16**, S33–S36 (2006)
- U. Chon, J.S. Shim, H.M. Jang, Compositional dependence of ferroelectric properties of highly c-axis oriented Bi_{4-x}Nd_xTi₃O₁₂ film capacitors. *Solid. State. Commun.* **129**, 465–468 (2004)
- X.Y. Mao, F.W. Mao, X.B. Chen, Ferroelectric and dielectric properties of Bi_{4-x}Nd_xTi₃O₁₂ ceramics. *Integr. Ferroelectr.* **79**, 155–161 (2006)

23. Y. Ahn, J.Y. Son, Mixed grains and orientation-dependent piezoelectricity of polycrystalline Nd-substituted $\text{Bi}_4\text{Ti}_3\text{O}_{12}$ thin films. *Ceram. Int.* **42**, 13061–13064 (2016)
24. F. Gao, H.F. Liu, F. Ren, K.T. Wang, X.S. Li, Y.B. Wang, C.L. He, Y.Z. Wei, Tunable structure and intensive upconversion photoluminescence for Ho^{3+} - Yb^{3+} codoped bismuth titanate composite synthesized by sol-gel-combustion (SGC) method. *Ceram. Int.* **46**, 3015–3022 (2020)
25. F.M. Yang, B. Jia, T. Wei, C.Z. Zhao, Q.J. Zhou, Z.P. Li, M.R. Du, M.C. Wang, Y.Y. Liu, C.Y. Xie, Reversible regulation of upconversion luminescence in new photochromic ferroelectric materials: $\text{Bi}_{4-x}\text{Er}_x\text{Ti}_3\text{O}_{12}$ ceramics. *Inorg. Chem. Front.* **6**, 2756–2766 (2019)
26. R. Bokolia, O.P. Thakur, V.K. Rai, S.K. Sharma, K. Sreenivas, Dielectric, ferroelectric and photoluminescence properties of Er^{3+} doped $\text{Bi}_4\text{Ti}_3\text{O}_{12}$ ferroelectric ceramics. *Ceram. Int.* **41**, 6055–6066 (2015)
27. K. Ruan, A. Gao, W. Deng, X. Chen, D. Bao, Orientation dependent photoluminescent properties of chemical solution derived $\text{Bi}_{4-x}\text{Eu}_x\text{Ti}_3\text{O}_{12}$ ferroelectric thin films. *J. Appl. Phys.* **104**, 036101 (2008)
28. D.P. Song, J. Yang, J.X. Sun, L.Y. Chen, J.K. Lee, Controlling the crystallization of Nd-doped $\text{Bi}_4\text{Ti}_3\text{O}_{12}$ thin-films for lead-free energy storage capacitors. *J. Appl. Phys.* **127**, 224102 (2020)
29. Y.Q. Gong, H.Y. Chen, S.H. Xie, X.J. Li, Effects of Nb Content on the ferroelectric and dielectric properties of Nb/Nd-Co-doped $\text{Bi}_4\text{Ti}_3\text{O}_{12}$ thin films. *J. Electron. Mater.* **47**, 1792–1797 (2018)
30. A. Marikani, V. Selvamurugan, G. Mangamma, S. Ravi, R. Krishnasharma, P.V. Chandrasekar, M. Kamruddin, D. Madhavan, Ferroelectric, dielectric, and optical properties of Nd-substituted $\text{Bi}_4\text{Ti}_3\text{O}_{12}$ nanoparticles synthesized by sol-gel method. *Prog. Nat. Sci.* **26**, 528–532 (2016)
31. M.S. Alkathy, F.L. Zabetto, M.H. Lente, J.A. Eiras, Octahedral distortion and oxygen vacancies induced band-gap narrowing and enhanced visible light absorption of Co/Fe co-doped $\text{Bi}_{3.25}\text{Nd}_{0.75}\text{Ti}_3\text{O}_{12}$ ferroelectrics for photovoltaic applications. *J. Phys. D: Appl. Phys.* **53**, 465106 (2020)
32. X.D. Li, Z.N. Chen, L.S. Sheng, Large enhancement of piezoelectric properties and resistivity in Cu/Ta co-doped $\text{Bi}_4\text{Ti}_3\text{O}_{12}$ high temperature piezoceramics. *J. Am. Ceram. Soc.* **102**, 7366–7375 (2019)
33. S.K. Badge, A.V. Deshpande, Effect of vanadium doping on structural, dielectric and ferroelectric properties of bismuth titanate ($\text{Bi}_4\text{Ti}_3\text{O}_{12}$) ceramics. *Ceram. Int.* **45**, 15307–15313 (2019)
34. X. Li, L. Zhu, P. Huang, Z. Chen, W. Bai, L. Li, F. Wen, P. Zhen, W.L. Wu, Y. Zheng, Reduction of oxygen vacancy concentration and large enhancement of electrical performances in Cu/Sb co-doped $\text{Bi}_4\text{Ti}_3\text{O}_{12}$ high temperature piezoelectric ceramics. *J. Appl. Phys.* **127**, 044102 (2020)
35. Q. Zhou, B.J. Kennedy, C. Howard, Structural studies of the ferroelectric phase transition in $\text{Bi}_4\text{Ti}_3\text{O}_{12}$. *Chem. Mater.* **15**, 5025–5028 (2003)
36. Y. Liu, L. Fan, W. Yi, C. Yan, J. Ma, Q. Ji, Q. Lin, Microstructure and ferroelectric properties of bi-excess $\text{Bi}_4\text{Ti}_3\text{O}_{12}$ thin films grown on Si and Pt/Ti/SiO₂/Si substrates. *Ferroelectrics* **54**, 144–149 (2020)
37. X. Du, W. Huang, S.K. Thatikonda, N. Qin, D. Bao, Improved ferroelectric and dielectric properties of Sm, La co-doped $\text{Bi}_4\text{Ti}_3\text{O}_{12}$ multifunctional thin films with orange-red emission. *J. Mater. Sci.-Mater. El.* **30**, 13158–13166 (2019)
38. D. Coathup, Z. Li, X. Zhu, H. Yan, R. Zhang, H. Ye, Dielectric and ferroelectric properties of BTFCO thin films. *J. Electroceram.* **43**, 92–95 (2019)
39. X. Hu, A. Garg, Z.H. Barber, Structural and electrical properties of samarium-substituted bismuth titanate ferroelectric thin films on Pt/TiOx/SiO₂/Si substrates. *Thin Solid Films* **484**, 188–195 (2005)
40. G. Xia, H. Tan, Ren, Effect of Fe substitution on microstructure and properties of bismuth titanate thin films. *Ceram. Int.* **42**, 1267–1271 (2016)
41. M.A. Islam, M.S. Islam, Synthesis and Characterization of La and Nd Co-doped bismuth titanate ferroelectric ceramics. *Int. J. Appl. Ceram. Tec.* **12**, E191–E196 (2015)
42. D. Zhou, H.S. Gu, Y.M. Hu, Z.L. Qian, Z.L. Hu, K. Yang, Y.N. Zou, Z. Wang, Y. Wang, J.G. Guan, W.P. Chen, Raman scattering, electronic, and ferroelectric properties of Nd modified $\text{Bi}_4\text{Ti}_3\text{O}_{12}$ nanotube arrays. *J. Appl. Phys.* **107**, 094105 (2010)
43. V.R. Prasad, M. Seshadri, S. Babu, Y.C. Ratnakaram, Concentration-dependent studies of Nd³⁺-doped zinc phosphate glasses for NIR photoluminescence at 105 μm . *Luminescence* **32**, 443–451 (2017)
44. M. Balestrieri, S. Colis, M. Gallart, G. Schmerber, A. Dinia, Photoluminescence properties of rare earth (Nd, Yb, Sm, Pr)-doped CeO₂ pellets prepared by solid-state reaction. *J. Mater. Chem. C* **3**, 7014–7021 (2015)
45. M. Pinatti, T.M. Mazzo, R.F. Gonçalves, J.A. Varela, E. Longo, I.L.V. Rosa, CaTiO₃ and Ca_{1-3x}Sm_xTiO₃: photoluminescence and morphology as a result of hydrothermal microwave methodology. *Ceram. Int.* **42**, 1352–1360 (2016)
46. S. Yang, J. Yao, Y. Quan, Monitoring the charge-transfer process in a Nd-doped semiconductor based on photoluminescence and SERS technology. *Light-Sci. Appl.* **9**, 117 (2020)
47. Y. Chen, C.H. Nie, Y.L. Bai, S.F. Zhao, The photovoltaic spectral response regulated by band gap in Zr doped $\text{Bi}_4\text{Ti}_3\text{O}_{12}$ thin films. *J. Mater. Sci.-Mater. El.* **26**, 5917–5922 (2015)

48. H. He, Z. He, Z. Jiang, J. Wang, T. Liu, N. Wang, A controllable photoresponse and photovoltaic performance in $\text{Bi}_4\text{Ti}_3\text{O}_{12}$ ferroelectric thin films. *J. Alloy. Compd.* **694**, 998–1003 (2017)
49. Y. Chang, C.S. Tu, P.Y. Chen, Raman vibrations and photovoltaic conversion in rare earth doped $(\text{Bi}_{0.93}\text{RE}_{0.7})\text{FeO}_3$ (RE=Dy, Gd, Eu, Sm) ceramics. *Ceram. Int.* **42**, 834–842 (2016)
50. S. Sharma, J.M. Siqueiros, O.R. Herrera, Structural, dielectric, ferroelectric and optical properties of Er doped BiFeO_3 nanoparticles. *J. Alloy. Compd.* **853**, 156979 (2021)

Publisher's Note Springer Nature remains neutral with regard to jurisdictional claims in published maps and institutional affiliations.